# Stabilizing perovskite solar cells with modified indium oxide electron transport layer

*Sergey Tsarev[a], Tatiana Dubinina[b,e], Selina Olthof[c], Antonio Guererro[d], Sergey Yu Luchkin[a], Keith J. Stevenson[a], Sergey M. Aldoshin[b], Juan Bisquert[d], and Pavel A. Troshin[b]*

A –Skolkovo Institute of Science and Technology, 121205, Moscow, Russia
B –Institute for Problems of Chemical Physics of the Russian Academy of Sciences (IPCP RAS), 142432, Chernogolovka, Russia
C – Department of Chemistry, University of Cologne, LuxemburgerStraße 116, 50939 Cologne, Germany.
D– Institute of Advanced Materials (INAM), UniversitatJaume I, 12006 Castello, Spain.
E – Faculty of Fundamental Physical and Chemical Engineering, Lomonosov Moscow State University, 119991, Moscow, Russia

## Abstract

Despite the impressive progress, the perovskite solar cells are still under the stage of laboratory research, mainly because of their inferior operational stability. To improve the device lifetime, one of the most important strategies is to eliminate the undesirable side reactions between the functional layers. In this study, we present the thermal oxidation method to yield high-quality pristine and modified indium oxide films applied as efficient electron transport layers (ETLs) for perovskite cells in a planar n-i-p configuration. The cells incorporating $In_2O_3$ as ETL material can deliver comparable efficiencies with the reference $SnO_2$-based devices while showing much superior operational stability. We attributed the observed stabilizing effect of indium oxide to its reduced chemical activity at the interface with the perovskite absorber layer. In particular, $In_2O_3$ can hardly oxidize $I^-$ to molecular iodine on the contrary to $SnO_2$ and $TiO_2$ known for their photocatalytic activity. We believe that this study may provide researchers with general guidelines to develop a large variety of ETL materials for efficient yet stable perovskite cells.

## Introduction

Perovskite photovoltaics is an emerging technology that potentially can rival silicon solar cells. The power conversion efficiency of perovskite solar cells (PSCs) rapidly increased from 3.2%[1] to striking 25.5%[2] in just a decade. Today, the commercialization of PSCs is mainly hindered by short operational lifetimes rather than by insufficient device efficiency[3,4]. Clearly, a bigger effort should be focused on understanding the degradation processes and developing more stable materials for improving the durability of perovskite solar cells.

Charge transport layers represent an essential functional part of any PSC architecture and have certain requirements to deliver high power conversion efficiency such as the optimal energy level alignment with the perovskite absorber, the low defect density in combination with good charge transport properties. While the instability of the PSCs is rather a complex problem, the chemical compatibility of the perovskite absorber and the adjacent charge transport layers especially has a profound impact on the device lifetime[2–4]. Unfortunately, the high power conversion efficiency of the solar cells does not necessarily guarantee their good operational stability. For instance, a widely used hole transport layer spiro-OMeTAD may introduce cell degradation through the diffusion of Li-containing dopants into the perovskite active

layer and parasitic reactions at the interface with the perovskite absorber[5,6]At the same time, titanium dioxide, a commonly used ETL material, introduces degradation at the interface with the perovskite absorber layer when exposed to UV light[7]. Therefore, particular attention has to be paid not only to the engineering of highly efficient solar cells but also to designing and implementation of appropriate charge transport interlayers enabling stable interfaces with the perovskite absorbers.

Currently, the most widely used ETL materials in n-i-p PSCs are represented by $SnO_2$, ZnO, and $TiO_2$. Among those, the $SnO_2$/perovskite interface is considered the most stable[8,9]. However, tin has three stable oxidation states $Sn^0$, $Sn^{2+}$, and $Sn^{4+}$, which trigger a rather complex set of possible redox reactions that may facilitate the degradation of the perovskite absorber. For instance, $SnO_2$ can catalyze the photooxidation of iodide[10]. Therefore, our approach to design more stable ETL materials was based on the selection of metals that form n-type oxides with strongly suppressed activity with respect to $I^-$ (photo)oxidation. The indium(III) oxide matches this requirement quite well, as indium +1 and +2 valence states are relatively unstable[11]. Indium (III) oxide has been used as ETL material in perovskite solar cells previously, but these devices delivered considerably reduced efficiencies as compared to the benchmark cells that can be easily produced using $SnO_2$ or $TiO_2$ ETLs [12–16].

In this study, we present thermally grown indium-based oxide films as high-quality ETL materials for efficient and stable perovskite solar cells. We employed thermal oxidation of evaporated metal films to obtain oxide layers with controllable properties, which resulted in a dramatic increase in solar cell performance. This study also assesses the effect of the electron transport layer composition on the stability of perovskite solar cells. We believe that this work will supply researchers with a general methodology of metal oxide fabrication that may facilitate the development of stable and efficient perovskite cells using a wide variety of rationally engineered ETL materials.

## Results and discussion

Growing chemically pure indium oxide films is crucial to investigate the stability of the interface of this oxide ETL with the perovskite absorber. Despite the appeal of the solution processing, it may introduce chemical impurities into the "oxide" films, such as alkali, halide, or organic impurities[17–19]. On the contrary, vacuum-based deposition methods can produce homogeneous and chemically pure films and also allow one to adjust the chemical composition of the film through a co-evaporation process (Figure 1A). Firstly, we used a relatively simple thermal deposition of indium metal followed by its conversion to indium oxide by annealing samples in the air at 400°C for 10 minutes. This method delivered uniform films with RMS of 3.2 nm, as evidenced by surface topography and conductivity scans (Figure 1C).

It was revealed that indium oxide coating improves the optical properties of ITO by increasing the transparency of the glass/ITO/$In_2O_3$ stack to a maximal 95% at 500 nm (Figure 2A). The tin dioxide layer also increased the transparency of the ITO substrates thus suggesting that both oxide coatings suppress light reflection from the ITO/air interface. Similar minimization of reflection losses should also be expected for complete cells with the perovskite absorber films deposited on the oxide ETLs.
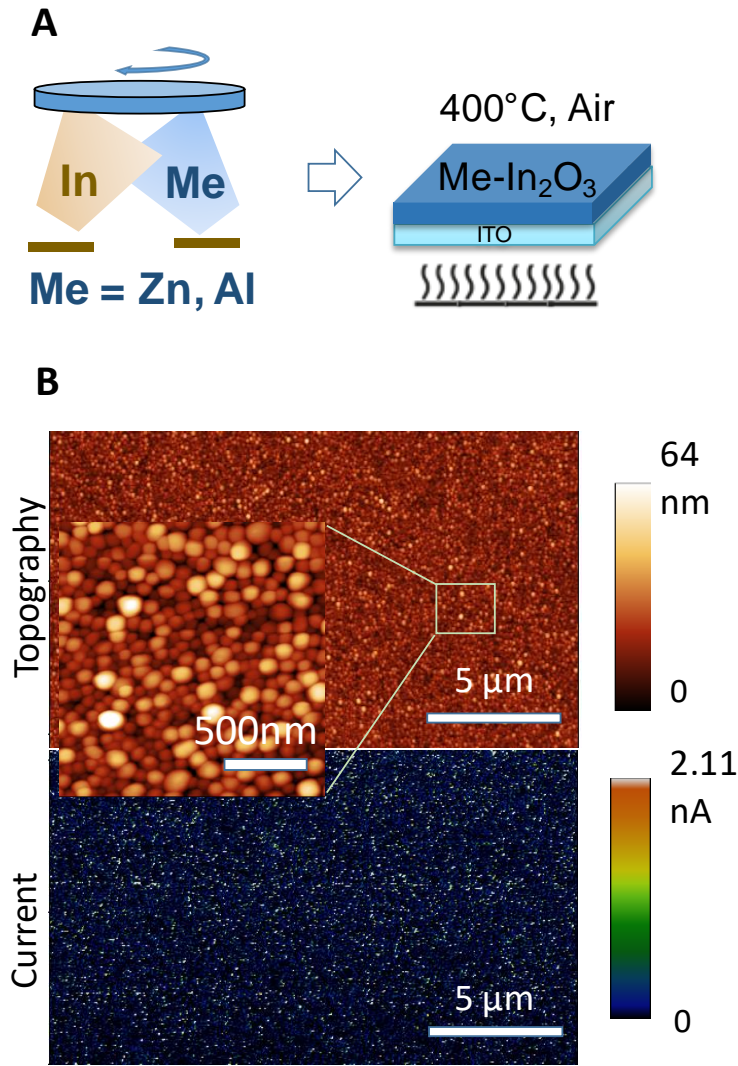
Figure 1. A. Schematics of indium oxide ETL fabrication. B. Topography and conductivity maps of 50 nm thick $In_2O_3$ films deposited on ITO

The steady-state photoluminescence (PL) measurements for glass/ITO/ETL/MAPbI$_3$ stacks indicated a stronger quenching of the perovskite absorber PL by $In_2O_3$ as compared to $SnO_2$ (Figure 2B). Enhanced absorber PL quenching may suggest a higher rate of electron extraction by the indium oxide if we follow the common interpretation of this effect.[20] However, such an assumption does not match the inferior photovoltaic performance of the cells incorporating $In_2O_3$ ETL. Alternatively, the higher photoluminescence intensity of perovskite deposited on tin oxide could show improved crystallization and lower concentration of the recombination centers resulting in more intense PL. Images of the absorber film topography also showed an increased grain size of the perovskite crystallized on indium oxide and rougher surface (21 nm versus 17 nm for the perovskite grown on tin oxide, Figure 2C).
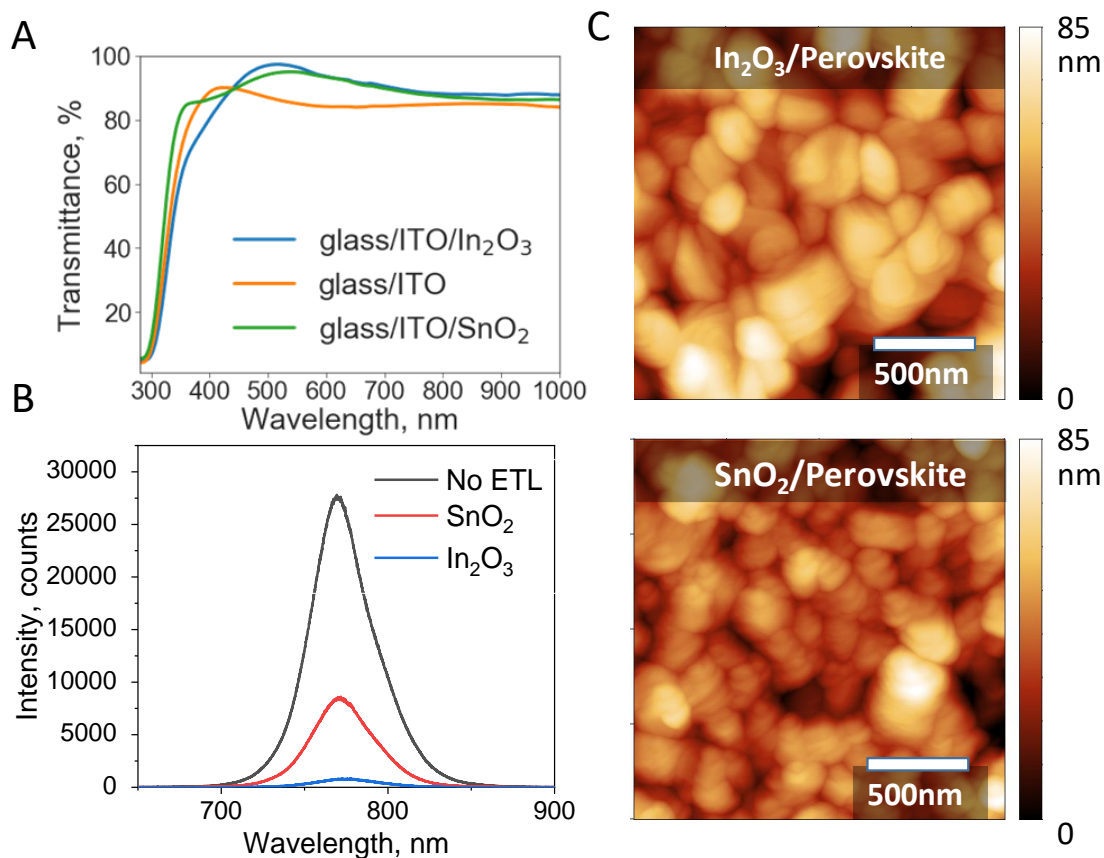
Figure 2. A. Optical transmittance of the glass/ITO/ETL stacks compared to the glass/ITO substrates. The thickness of $In_2O_3$ equals to 50 nm, the thickness of $SnO_2$ equals to 80 nm B. Photoluminescence of $MAPbI_3$ films grown above $In_2O_3$ and $SnO_2$ ETLs C) Topography scans of perovskite films grown on $In_2O_3$ and $SnO_2$

A straightforward approach to evaluate any emerging ETL material is to compare it with a known well-performing benchmark[21][20]. Nanocrystalline tin dioxide films obtained from a commercial $SnO_2$ sol represent a very popular electron transport layer capable of delivering highly efficient perovskite solar cells. Therefore, we compared the performance of our thermally grown $In_2O_3$ films with the reference $SnO_2$ ETL in n-i-p planar PSCs. The device configuration was ITO/ETL/PCBA/$MAPbI_3$/PTA/Polystyrene(PS)/$MoO_3$/Al (Figure 3C). I t should be noticed that all oxide ETLs were additionally coated with a monolayer of the fullerene derivative phenyl-$C_{61}$-butyric acid (PCBA) serving as a defect passivation layer[22]. The cells without such passivation are slightly less efficient as shown in figure S1 (Supporting information, SI).

We optimized the thickness of the ETL and found that 50 nm thick films of $In_2O_3$ deliver the best performance as illustrated in figure 3A. The best (average) cell with the optimized thickness of $In_2O_3$ delivered open circuit voltage ($V_{OC}$) of 1023 (976) mV, short circuit current density ($J_{SC}$) of 21.4 (21.5) mA $cm^{-2}$, fill factor (FF) of 75% (62%) and power conversion efficiency (PCE) of 16.5% (13.1%) when measured in the reverse (forward) direction. To compare, the current-voltage characteristics of the reference perovskite solar cells with $SnO_2$ ETL were practically hysteresis-free and delivered $V_{OC}$ of 1116 mV, $J_{SC}$ of 22.4 mA $cm^{-2}$, FF of 81%, and PCE of 20.3% expectedly confirming the superior performance of this well-established benchmark system. However, it is worth noting that the devices with thermally-grown $In_2O_3$ demonstrated a comparable performance with the best of the previously reported PSCs using $In_2O_3$ ETL processed by other methods[15,16,23]. Therefore, we conclude that the thermal evaporation followed by

thermal oxidation of metallic indium films is a promising approach for the deposition of high-quality indium oxide films.
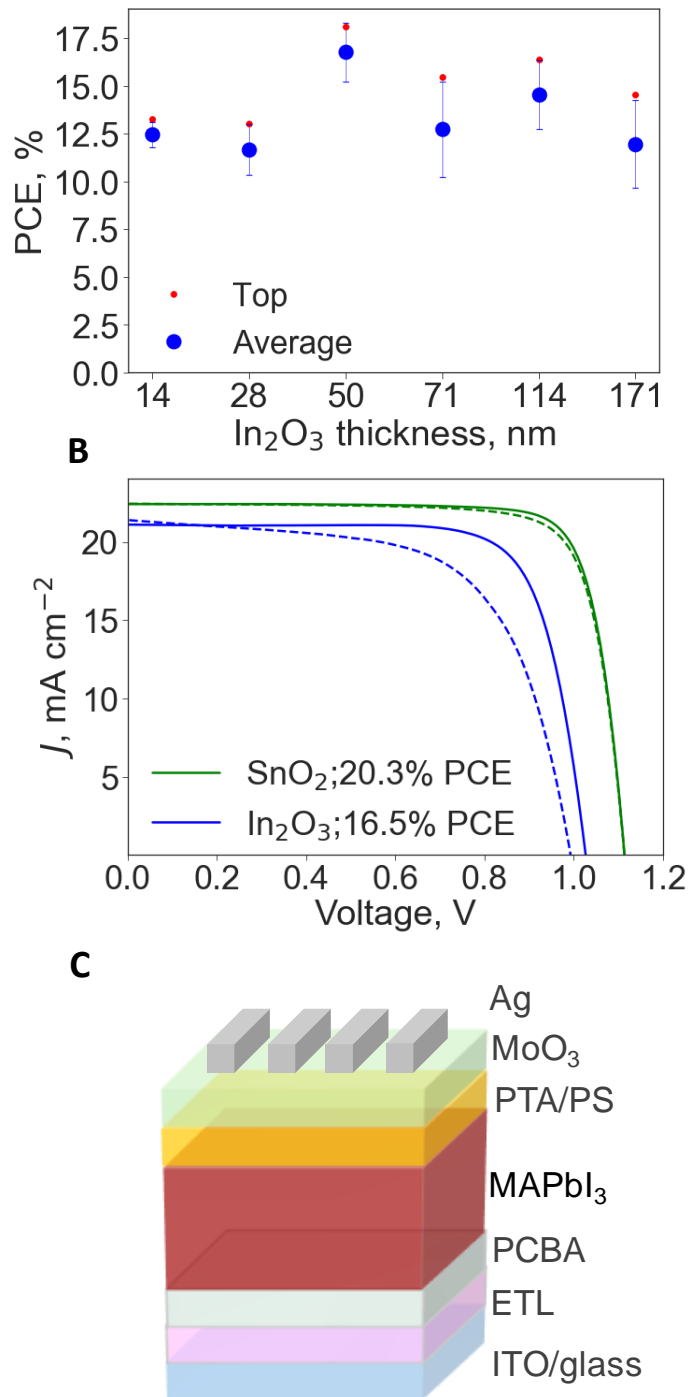


Figure 3. A. Power conversion efficiencies of ITO/In$_2$O$_3$/PCBA/MAPbI$_3$/PTA/PS/MoO$_3$/Ag perovskite solar cells depending on the ETL thickness B. I-V curves of the top cells with In$_2$O$_3$ and SnO$_2$ETLs measured in forward and reverse directions with 20mVs$^{-1}$voltage sweeping rate. C. Solar cell structure

A big advantage of the proposed thermal growth method is a possibility for straightforward and well-controlled modification of the chemical composition and electronic properties of In$_2$O$_3$ films e.g. by co-evaporation of multiple metals while forming the precursor films. In this study, we selected samarium, tin, zinc, and aluminum and co-evaporated them together with indium at the rates $U_M : U_{In} = 0.05 : 0.95$

5

Å/sec. The deposited films were then converted to oxides by sintering them in the air at 400°C in the same manner as for the pristine $In_2O_3$. The thickness of the final oxide coating was 50 nm in all cases.

The modified $In_2O_3$ films were evaluated as ETLs in the same PSC configuration as above. Using tin and samarium as modifying metals slightly improved the device performance as compared to the pristine $In_2O_3$. However, we observed a large variation of the cell parameters pointing to the reduced reproducibility. Loading indium oxide ETLs with aluminum and zinc as modifiers improved $V_{OC}$, fill factors, and overall device performance. The overview of the photovoltaic performances, external quantum efficiency spectra, and I-V curves are shown in figure 4, while the statistics on the PCE variation is presented in table 1. The best solar cells with Al and Zn as ETL modifiers delivered PCEs of 18.6%/15.9% and 18.7%/15.4% when measured in the reverse/forward directions, respectively. Importantly, the modification of indium oxide with aluminum and zinc improved the reproducibility of the solar cell fabrication process. For the indium-aluminium and indium-zinc oxides, all of the devices showed comparable PV performances, while in the case of using bare indium oxide some cells were shorted.
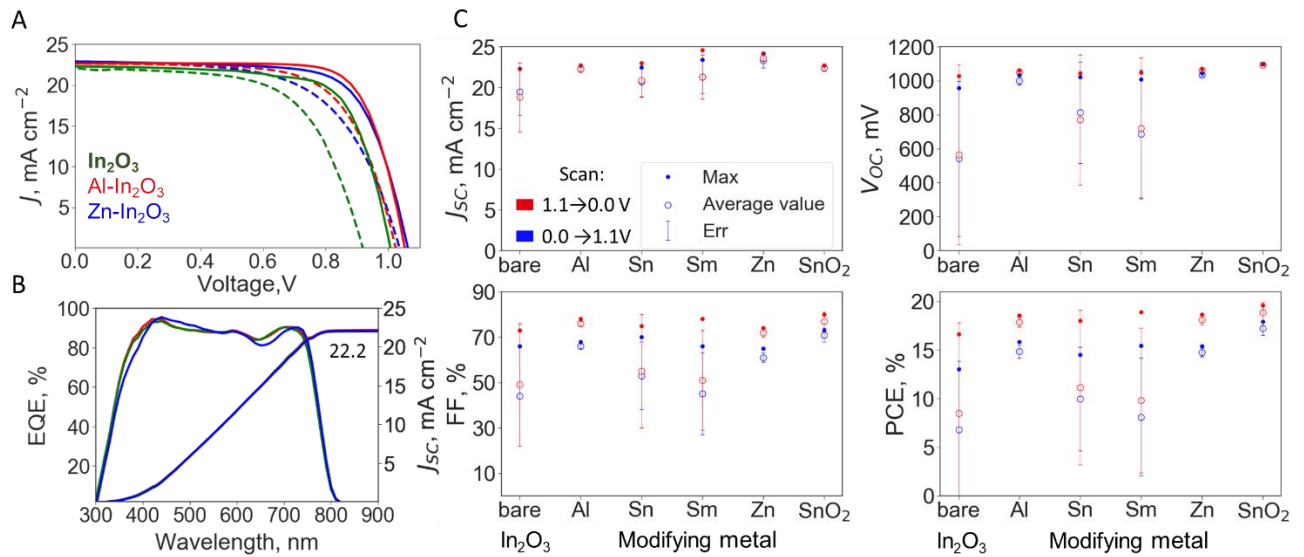


Figure 4. A. Representative I-V curves of the ITO/ETL/PCBA/MAPbI$_3$/PTA/PS/MoO$_3$/Al perovskite solar cells with ETLs based on bare $In_2O_3$ and the oxide modified with other metals. B. EQE spectra of the corresponding solar cells C. Distribution of the device parameters with ETLs based on pristine and modified $In_2O_3$ compared with the reference cells with $SnO_2$ ETL

Table 1. The performance parameters of the ITO/ETL/PCBA/MAPbI$_3$/PTA/PS/MoO$_3$/Al perovskite solar cells with ETLs based on bare In$_2$O$_3$ and modified with other metals. The PV parameters are represented in a form of (top) average ± standard deviation.

| | V$_{OC}$, mV | J$_{SC}$, mA cm$^{-2}$ | FF, % | PCE, % | Scan direction |
|---|---|---|---|---|---|
| In$_2$O$_3$ | (966) 906±46.8* | (23.1) 20.3±1.9* | (65.8) 59.6±6.1* | (13.3) 10.9±1.3* | FWD |
| | (1027) 976±35.9* | (23.0) 21.1±1.6* | (77.0) 67.7±10.0* | (17.4) 13.9±2.4* | REV |
| Zn-In$_2$O$_3$ | (1046) 1033±10* | (24.2) 23.3±0.9* | (65)61±2* | (15.4) 14.8±0.4* | FWD |
| | (1071) 1061±9* | (24.2) 23.6±0.4* | (74)73±2* | (18.7) 18.1±0.5* | REV |
| Al-In$_2$O$_3$ | (1033) 1001±23* | (22.7) 22.3±0.4* | (68)66±1* | (15.9) 14.8±0.7* | FWD |
| | (1062) 1050±10* | (22.7) 22.3±0.4* | (78)76±1* | (18.6) 17.9±0.5* | REV |

*For pure indium oxide ETL, due to large batch-to-batch and device-to-device variation, we present the data for 26 devices from 4 batches of solar cells. For the modified oxides the data is presented from 8 cells in total*

Furthermore, we investigated the effect of the perovskite absorber composition on the efficiency of the solar cells with Al-In$_2$O$_3$ and SnO$_2$ ETL materials. Replacing MAPbI$_3$ with the methylammonium-free Cs$_{0.12}$FA$_{0.88}$PbI$_3$ perovskite and using conventional SnO$_2$ ETL delivered V$_{OC}$ of 1080 mV, J$_{SC}$ of 23.2 mA cm$^{-2}$, FF of 74% and PCE of 18.7% when measured in reverse voltage sweep direction. The solar cells with Al-In$_2$O$_3$ demonstrated comparable performance with V$_{OC}$ of 1075 mV, J$_{SC}$ of 23.4 mA cm$^{-2}$, fill factor of 76% and PCE of19.3% when measured under the same conditions. These results show that the Al-In$_2$O$_3$ ETL can deliver at least comparable power conversion efficiencies as the SnO$_2$ ETL in combination with the methylammonium-free perovskite absorber. The IV curves and data are demonstrated in the SI, figure S2, table S2.

Ultraviolet photoelectron spectroscopy (UPS) measurements were used to check the energy level alignment of lead halide perovskites with pristine and modified In$_2$O$_3$-based ETL materials. The glass/ITO/In$_2$O$_3$, ITO/Al-In$_2$O$_3$, glass/ITO/In$_2$O$_3$/MAPbI$_3$ and glass/ITO/In$_2$O$_3$/Cs$_{0.12}$FA$_{0.88}$PbI$_3$ stacks were studied using a previously reported methodology[24]. We observed that the conduction band (CB) of pristine indium oxide is misaligned by>0.2eV with respect to CBs of both perovskite absorbers (table S1). Such unfavorable band alignment may explain the lower V$_{OC}$ and the pronounced hysteresis of the cells fabricated with the pristine In$_2$O$_3$ ETL. On the contrary, the Al-In$_2$O$_3$ showed a significantly improved band alignment with CB positioned at 3.9 eV, which almost perfectly matches the CB position of the perovskite absorbers (figure 5). These findings explain the superior performance of the perovskite solar cells assembled with the modified Al-In$_2$O$_3$ ETL as compared to the reference cells with pristine In$_2$O$_3$.
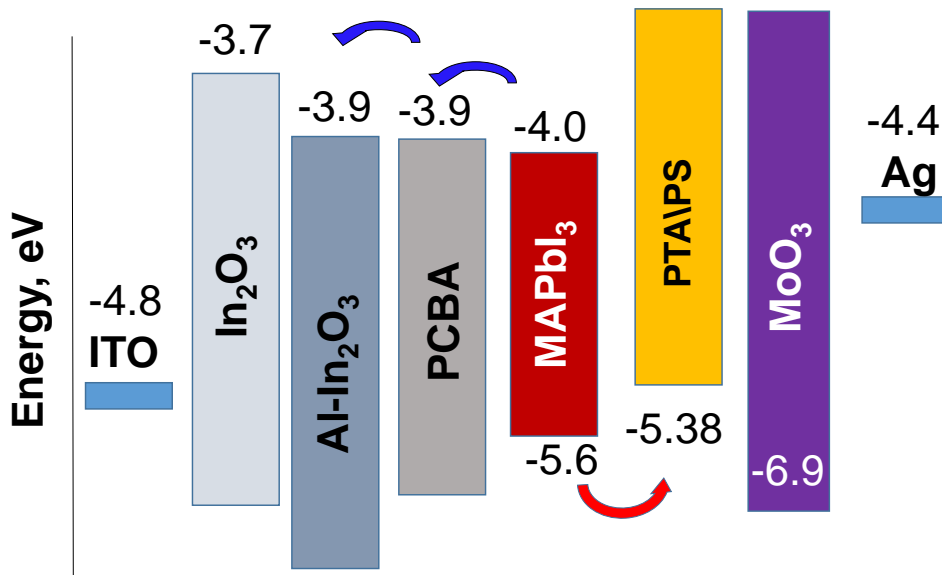
Figure 5. Band diagram for the perovskite solar cell layout. Energy values are taken from[33–35], or measured using UPS (indium oxides and perovskite).

To investigate the operation stability of PSCs, we fabricated a special set of devices with the ITO/ETL/MAPbI$_3$/HTL/MoO$_3$/Al configuration. The MoO$_3$/Al hole-selective contacts were used because of their excellent encapsulation properties as compared to the MoO$_3$/Ag.[29] Suppressing the degradation of top contact and absorber/HTL interface was crucial for monitoring the aging effects associated with the ETL/perovskite interface or the perovskite layer itself. The fabricated cells were exposed to 50 mW/cm$^2$ white light provided by metal halide lamps under a nitrogen atmosphere inside the glove box, whereas the sample temperature was equilibrated at 65°C. All devices were non-encapsulated, aged under open-circuit conditions and their PV parameters were regularly tracked.

Figure 6 shows that the reference solar cells with the SnO$_2$ ETL rapidly degraded losing more than 80% of their initial efficiency within 1000 h of aging. These results were quite surprising since SnO$_2$ reportedly forms one of the most stable interfaces with the lead halide perovskites[8], therefore one could expect that devices with SnO$_2$ should survive for more than 1000 h. However, the analysis of the reported degradation experiments leads to the conclusion that most of them were implemented at low temperatures and often UV filters were used[8,9,30]. Most likely, temperature control and UV-free illumination are essential prerequisites to achieve long-term stability for PSCs incorporating the SnO$_2$/perovskite interface[31]. However, the solar cells designed for realistic practical applications should withstand both high temperatures and light with a natural fraction of UV photons.

In that context, the devices assembled using In$_2$O$_3$ ETL look much more promising since they display largely enhanced operational stability. The modification of In$_2$O$_3$ with Zn compromised the PSCs stability as can be concluded from nearly 60% loss of the initial performance by 1000 h of aging. Presumably, the observed accelerated degradation is due to the known parasitic reaction of ZnO with MAPbI$_3$[32]. On the contrary, the devices with Al-In$_2$O$_3$ ETL showed the best stability retaining nearly 90% of the initial PCE after 1000 h of photothermal aging.
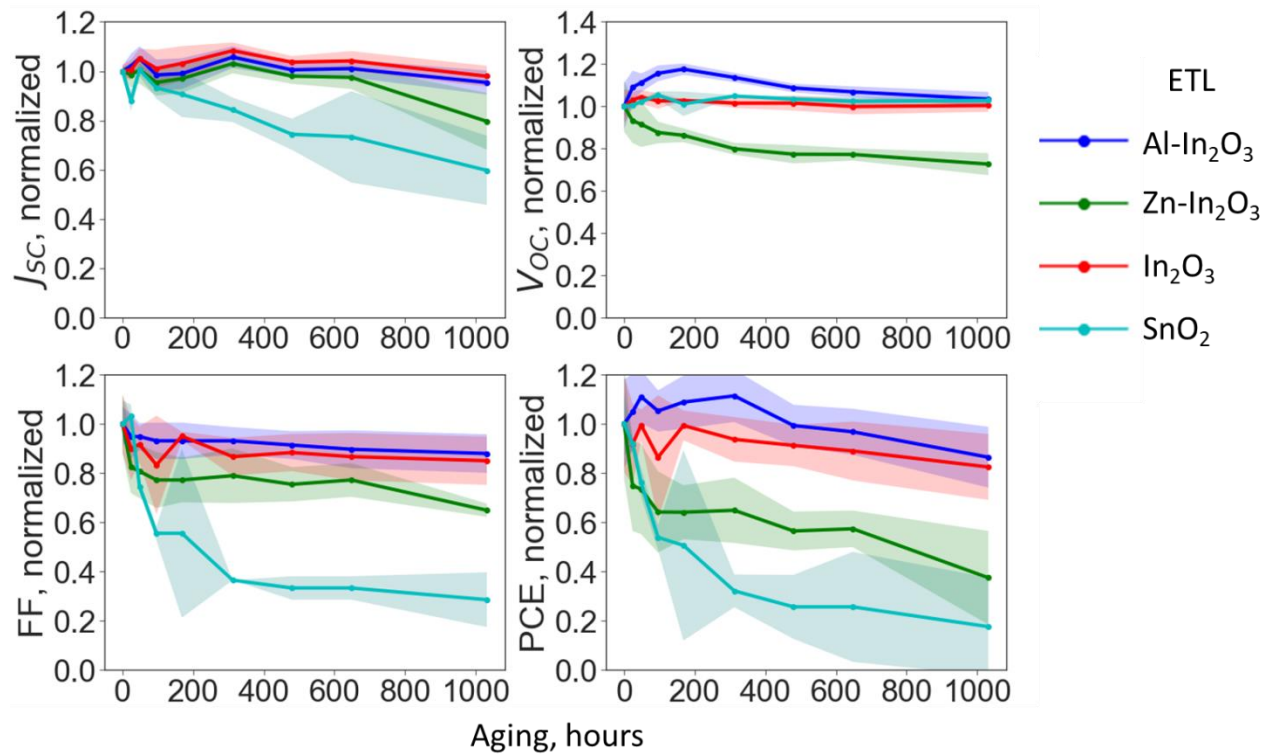
Figure 6. Evolution of the normalized solar cell parameters under continuous white light illumination (50mWcm$^{-2}$) at 65°C in an inert $N_2$ atmosphere. The device configuration was ITO/ETL/MAPbI$_3$/PTA/MoO$_3$/Al, where ETL was SnO$_2$, In$_2$O$_3$, Zn-In$_2$O$_3$ or Al-In$_2$O$_3$. The parameters were averaged for 8 devices of each configuration and the standard deviation is highlighted with colored areas.

To gain more insights on the degradation processes occurring in the ETL/perovskite interface, we performed an impedance spectroscopy study on an additional set of samples degraded at MPP tracking conditions whilst intercalating IS measurements at different times (Fig. 7). For this study, the device architecture was ITO/ETL/MAPbI$_3$/PTA/PS/MoO$_3$/Al, where ETL was either SnO$_2$ or Al-In$_2$O$_3$. The degradation time was limited to 140 hours at MPP conditions (Fig. 7a) since degradation for the SnO$_2$ was already very severe. The dashed line indicates the efficiency of the samples at which the final impedance spectra were recorded. The reference cell using tin oxide as ETL severely degrades in the initial 20 h to below 50% of the initial efficiency from 14.2% to 6.8%. Alternatively, the device containing the Al-In$_2$O$_3$ is more stable and after 140 h of aging the cell retains about 80% of the initial efficiency with absolute values ranging from 14 % to 11.1 %. Selected Impedance spectroscopy spectra measured during the first 18 h are shown in Fig. 7b and 7c for devices containing SnO$_2$ and Al-In$_2$O$_3$ ETLs, respectively. The impedance spectroscopy measurements were recorded in-line every 13 minutes at the $V_{DC}$ needed to keep the MPP condition. Fresh samples show two arcs in the complex impedance plots as expected for high-efficiency hybrid perovskites. The high frequency (HF) arc of a fresh sample usually offers information on the bulk properties of the perovskite and recombination of photogenerated carriers with some contribution from the contacts[33]. In this case, the contribution of the contacts for the SnO$_2$ sample is very high since the initial HF resistance is ~428 $\Omega$ and the HF resistance of Al-In$_2$O$_3$ is only ~71 $\Omega$, using the same illumination and bias conditions. Previous degradation experiments carried out under illumination conditions concluded that degraded interfaces show an increase in the HF resistance[34]. Here this is the case for the SnO$_2$ sample showing an increase from ~428 $\Omega$ to ~892 $\Omega$. This is a clear effect of an increase in the charge transfer resistance at that interface or to an increase in the transport resistance at the new species generated at that contact.
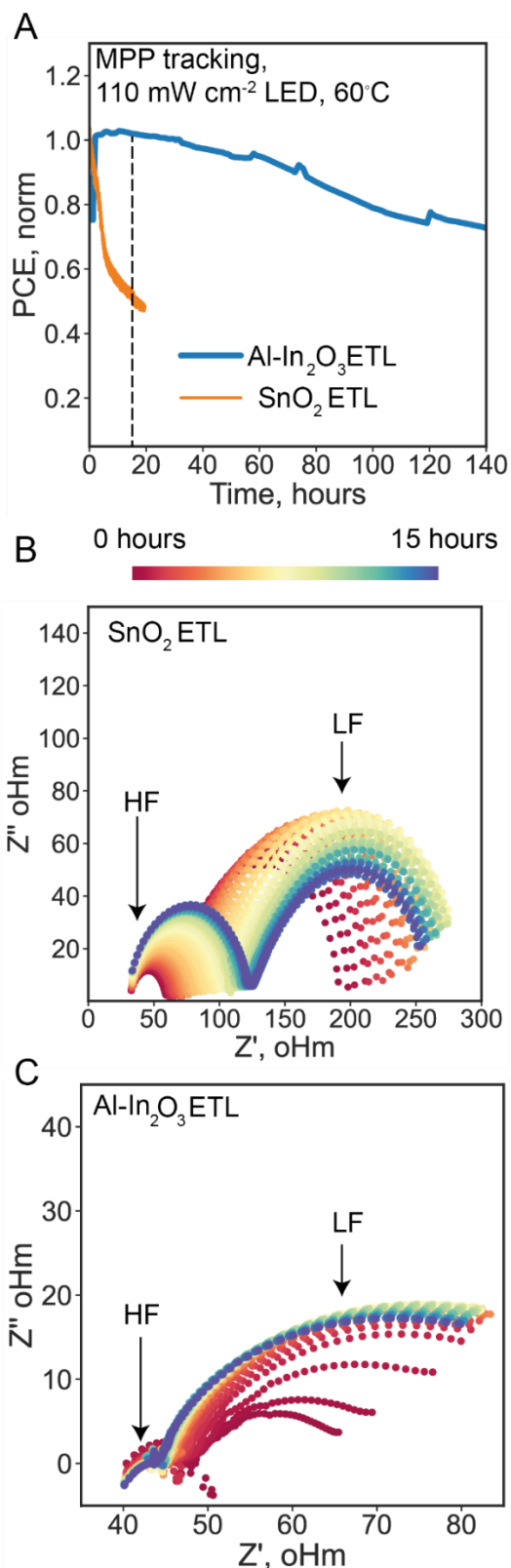
Figure 7. A. MPPT Tracking results for the ITO/ETL/MAPbI$_3$/PTA/PS/MoO$_3$/Al cells, where ETL is represented by Al-In$_2$O$_3$ or SnO$_2$. The cells were tracked at 60◦C and 110 mW/cm$^2$ white LED light, which stands for ~1.9 sun light exposure if normalized by perovskite absorption. Impedance spectra (B-C) were measured at V$_{mpp}$ every 15 minutes

A very different tendency is observed for the sample prepared with $In_2O_3$ where the HF resistance almost remains constant at values of ~71 $\Omega$. Alternatively, the low-frequency (LF) arc offers information on the perovskite/contacts interface and recombination of charge carriers. In the case of $SnO_2$-based devices, the LF resistance drops during the degradation process from ~1428 $\Omega$ to ~892 $\Omega$ as a result of the increased recombination of carriers due to inadequate charge extraction. Finally, the origin in the increase in the LF resistance of the $In_2O_3$ sample from ~178 $\Omega$ to ~285 $\Omega$ is not totally clear and requires further experiments. Presumably, it could be related to a reduction in the recombination kinetics of this sample probably affected by a paralell degradation pathway. Overall, the observed tendency in the IS response for the two different types of samples clearly point to different degradation mechanims, whilst the $SnO_2$-based cell shows a clear interfacial degradation related to the contact, whereas the $In_2O_3$ system shows a different type of degradation pathway i.e. modification of the perovskite itself.

## Conclusion

In this study, we presented a thermal growth method for the fabrication of high-quality films of pristine indium (III) oxide and $InO_x$ films modified with the oxides of other metals such as aluminum or zinc. High optical transparency and uniform coating of indium oxide films facilitated their application as electron transport layers in planar n-i-p perovskite solar cells. Using bare $In_2O_3$ as ETL delivered maximal PCE of 16.2%, whereas modified $Al-In_2O_3$ delivered maximal PCEs of 18.6% and 19.3% in combination with $MAPbI_3$ and $Cs_{0.12}FA_{0.88}PbI_3$ perovskite absorbers, respectively. Furthermore, the cells with $In_2O_3$ and $Al-In_2O_3$ demonstrated significantly improved operational stability maintaining nearly 90% of the initial PCE after 1000 h of continuous illumination under harsh open-circuit conditions at 65°C. We strongly believe that the developed in this work methodology can be extensively utilized in the rational design of new metal oxide-based ETLs with tailored properties for stable and efficient perovskite cells.

## Acknowledgments

## Experimental Section

**Preparation of perovskite inks:**
The inks were prepared in a nitrogen-filled glovebox using anhydrous solvents and dry powders. For the $MAPbI_3$ ink MAI (0.222 g) and $PbI_2$ (0.645 g) were dissolved in a mixture of DMF (0.800 mL) and NMP (0.200 mL). The precursor solutions were heated at 80°C for an hour and then filtered through a 0.45 µm PTFE syringe filter.
For the $Cs_{0.12}FA_{0.88}PbI_3$ ink, CsI (99 mg), FAI (435 mg) and $PbI_2$ (1474 mg) were mixed in DMF (1.7 mL) and DMSO (0.3 mL). The ink was dissolved by magnetic stirring at room temperature, filtered through a 0.45 µm PTFE syringe filter, and used within a day after the preparation.
**Solar cell fabrication**
Glass/ITO substrates (Kintec, 15 $\Omega$/sq.) were sequentially cleaned with toluene, acetone, and isopropanol. For indium oxide deposition, indium was evaporated under the pressure of 1 $10^{-5}$ torr with a rate of 1Å/sec. After the deposition, substrates were annealed in a furnace at 400°C for 10 minutes. Further steps were done in accordance with our previously published procedures[22,35]. For $SnO_2$ deposition, the tin dioxide

layer was obtained by spin-coating 10% aqueous tin dioxide suspension (Alfa-Aesar) at 4000 rpm for 40 s followed by annealing in air at 165°C for 15 minutes. All subsequent steps were performed under an inert atmosphere inside a nitrogen-filled glove box. If used, the solution of PCBA (0.2 mg/mL) in toluene was spin-coated on the ETLs at 3000 rpm. The samples were then annealed at 100°C for 5 minutes. The $MAPbI_3$ 1.4 M ink (70 μL) was spin-coated at 4000 rpm and quenched with toluene (130 μL) dropped 18 seconds after the start of spin-coating. The $Cs_{0.12}FA_{0.88}PbI_3$ was spin-coated at 4000 rpm (80 μL) and quenched with ethyl acetate (180 μL) dropped 15 seconds later. The deposited films were annealed for 10 minutes at 100°C on a hotplate. To passivate the surface of $Cs_{0.12}FA_{0.88}PbI_3$, MAI (0.030M) solution in anhydrous isopropanol was spin-coated at 4000 rpm for 10 seconds, followed by immediate annealing of substrates for 30 seconds at 100°C on a hotplate.

To deposit the HTL, PTA (poly[bis(4-phenyl)(4-methylphenyl)amine], 4 mg) in toluene (1 mL) was spin-coated at 1000 rpm on top of the perovskite films. Then, a solution of polystyrene (0.4 mg ml$^{-1}$) in ethyl acetate was spin-coated at 3000 rpm. Molybdenum oxide (15 nm)/Al (100 nm) electrodes were evaporated through a shadow mask. The device active area was 0.08 cm$^2$ as defined by the shadow mask.

**Characterization techniques**[22,35].

The current-voltage characteristics of the devices were measured under a nitrogen atmosphere using the simulated AM1.5G illumination (100 mW cm$^{-2}$) provided by Newport Verasol AAA class solar simulator. The intensity of the illumination was checked before each measurement using a calibrated silicon diode with a known spectral response. J–V curves were recorded using Advantest 6240A source-measurement units. The EQE spectra were measured using a PV Instruments system integrated with an MBraun glove box.

The absorption spectra were obtained in an inert atmosphere using AvaSpec-2048-2 fiber spectrometer integrated with an MBraun glove box. Atomic force microscopy measurements were performed in a semi-contact mode using ASYELEC-01probes and Cypher ES atomic force microscope installed in an Ar-filled MBraun glove box.

**Photoelectron spectroscopy measurements**

The measurements were performed on a custom-designed multi-chamber UHV system at a base pressure of $5 \cdot 10^{-10}$ mbar using a Phoibos 100 hemispherical analyzer (Specs) under normal emission to the sample. The electron binding energy scale EB is calibrated using the Fermi edge of cleaned gold substrates. UPS measurements were conducted with a helium discharge lamp (He I @ 21.22 eV, sample bias − 8 V) at a pass energy of 2 eV, with an energy resolution (as determined by the width of Fermi edge) of 110 meV. For XPS experiments, a Mg Kα excitation source was used (hv = 1252.6 eV) at a pass energy of 10 eV; the energy resolution is 800 meV.

**Impedance spectroscopy measurements:**

The impedance measurements were carried out using MFIA impedance analyzer by Zurich instruments. The scans were performed periodically in the frequency range of 1MHz to 1Hz with AC signal of 50mV and DC voltage bias equal to Vmpp. The Vmpp was tracked simultaneously on a different device with the same architecture. Each scan took about 13 minutes to complete. The scans were collected at 60∘C and 110 mW/cm$^2$ white LED light, which stands for the light bias formally equal to ~1.9 sun if normalized by the perovskite absorption. Faraday cage and foil-wrapped cables were used to minimize electromagnetic noise. The solar cell active area was 0.14 cm$^2$ for all of the devices.

# References

[1]     A. Kojima, K. Teshima, Y. Shirai, T. Miyasaka, *J. Am. Chem. Soc.* **2009**, *131*, 6050.

[2]     "NREL Chart," can be found under https://www.nrel.gov/pv/cell-efficiency.html, **n.d.**

[3]     A. F. Akbulatov, S. Y. Luchkin, L. A. Frolova, N. N. Dremova, K. L. Gerasimov, I. S. Zhidkov, D. V Anokhin, E. Z. Kurmaev, K. J. Stevenson, P. A. Troshin, *J. Phys. Chem. Lett.* **2017**, *8*, 1211.

[4]     H. S. Kim, J. Y. Seo, N. G. Park, *ChemSusChem* **2016**, *9*, 2528.

[5]     A. G. Boldyreva, A. F. Akbulatov, M. Elnaggar, S. Y. Luchkin, A. V. Danilov, I. S. Zhidkov, O. R. Yamilova, Y. S. Fedotov, S. I. Bredikhin, E. Z. Kurmaev, K. J. Stevenson, P. A. Troshin, *Sustain. Energy Fuels* **2019**, *3*, 2705.

[6]     A. K. Jena, Y. Numata, M. Ikegami, T. Miyasaka, *J. Mater. Chem. A* **2018**, *6*, 2219.

[7]     W. Li, W. Zhang, S. Van Reenen, R. J. Sutton, J. Fan, A. A. Haghighirad, M. B. Johnston, L. Wang, H. J. Snaith, *Energy Environ. Sci.* **2016**, *9*, 490.

[8]     J. A. Christians, P. Schulz, J. S. Tinkham, T. H. Schloemer, S. P. Harvey, B. J. Tremolet De Villers, A. Sellinger, J. J. Berry, J. M. Luther, *Nat. Energy* **2018**, *3*, 68.

[9]     Y. Hou, X. Du, S. Scheiner, D. P. McMeekin, Z. Wang, N. Li, M. S. Killian, H. Chen, M. Richter, I. Levchuk, N. Schrenker, E. Spiecker, T. Stubhan, N. A. Luechinger, A. Hirsch, P. Schmuki, H. Steinrück, R. H. Fink, M. Halik, H. J. Snaith, C. J. Brabec, *Science (80-. ).* **2017**, *358*, 1192.

[10]    C. Karunakaran, P. Anilkumar, P. Gomathisankar, *Chem. Cent. J.* **2011**, *5*, 1.

[11]    Loren G. HeplerZ Z. Hugus Jr.Wendell M. Latimer, *J. Am. Chem. Soc.* **1953**, *75*, 5652.

[12]    P. Chen, X. Yin, M. Que, Y. Yang, X. Liu, W. Que, *J. Alloys Compd.* **2018**, *735*, 938.

[13]    A. Apostolopoulou, D. Sygkridou, A. Rapsomanikis, A. N. Kalarakis, E. Stathatos, *Sol. Energy Mater. Sol. Cells* **2017**, *166*, 100.

[14]    L. Wang, F. Liu, X. Cai, T. Ma, C. Jiang, *J. Phys. Chem. C* **2018**, *122*, 28491.

[15]    M. Qin, J. Ma, W. Ke, P. Qin, H. Lei, H. Tao, X. Zheng, L. Xiong, Q. Liu, Z. Chen, J. Lu, G. Yang, G. Fang, *ACS Appl. Mater. Interfaces* **2016**, *8*, 8460.

[16]    S. Yoon, S. J. Kim, H. S. Kim, J. S. Park, I. K. Han, J. W. Jung, M. Park, *Nanoscale* **2017**, *9*, 16305.

[17]    L. Huang, X. Sun, C. Li, J. Xu, R. Xu, Y. Du, J. Ni, H. Cai, J. Li, Z. Hu, J. Zhang, *ACS Appl. Mater. Interfaces* **2017**, *9*, 21909.

[18]    L. J. Brillson, Y. Lu, *J. Appl. Phys.* **2011**, *109*, 121301.

[19]    F. Qin, W. Meng, J. Fan, C. Ge, B. Luo, R. Ge, L. Hu, F. Jiang, T. Liu, Y. Jiang, Y. Zhou, *ACS Appl. Mater. Interfaces* **2017**, *9*, 26045.

[20]    Q. Jiang, L. Zhang, H. Wang, X. Yang, J. Meng, H. Liu, Z. Yin, J. Wu, X. Zhang, J. You, *Nat. Energy* **2016**, *2*, 16177.

[21]    M. Ulfa, P. Wang, J. Zhang, J. Liu, W. D. De Marcillac, L. Coolen, S. Peralta, T. Pauporté, *ACS Appl. Mater. Interfaces* **2018**, *10*, 35118.

[22]    S. A. Tsarev, T. Dubinina, S. Y. Luchkin, I. S. Zhidkov, E. Z. Kurmaev, K. J. Stevenson, P. A. Troshin, *J. Phys. Chem. C* **2020**, *124*, 1872.

[23]    X. Guo, Z. Lin, J. Ma, Z. Hu, J. Su, C. Zhang, J. Zhang, J. Chang, Y. Hao, *J. Power Sources* **2019**, *438*, 226981.

[24]    S. Olthof, K. Meerholz, *Sci. Rep.* **2017**, *7*, 1.

[25]    R. T. White, E. S. Thibau, Z. H. Lu, *Sci. Rep.* **2016**, *6*, 1.

[26]    T. S. Sherkar, C. Momblona, L. Gil-Escrig, J. Ávila, M. Sessolo, H. J. Bolink, L. J. A. Koster, *ACS Energy Lett.* **2017**, *2*, 1214.

[27]    K. Wang, J. Feng, X. Zhu, S. Priya, C. Wu, S. Liu, X. Ren, R. Yang, D. Yang, G. Fang, *Nat. Commun.* **2018**, *9*, 3239.

[28]    W. Zhang, J. Xiong, L. Jiang, J. Wang, T. Mei, X. Wang, H. Gu, W. A. Daoud, J. Li, *ACS Appl. Mater. Interfaces* **2017**, *9*, 38467.

[29]    E. M. Sanehira, B. J. Tremolet De Villers, P. Schulz, M. O. Reese, S. Ferrere, K. Zhu, L. Y. Lin, J. J. Berry, J. M. Luther, *ACS Energy Lett.* **2016**, *1*, 38.

[30]    Q. Liu, M. C. Qin, W. J. Ke, X. L. Zheng, Z. Chen, P. L. Qin, L. Bin Xiong, H. W. Lei, J. W. Wan, J. Wen, G. Yang, J. J. Ma, Z. Y. Zhang, G. J. Fang, *Adv. Funct. Mater.* **2016**, 6069.

[31]    P. Hang, J. Xie, G. Li, Y. Wang, D. Fang, Y. Yao, D. Xie, C. Cui, K. Yan, J. Xu, D. Yang, X. Yu, *iScience* **2019**, *21*, 217.

[32]    K. Schutt, P. K. Nayak, A. J. Ramadan, B. Wenger, Y. H. Lin, H. J. Snaith, *Adv. Funct. Mater.* **2019**, *29*, 1900466.

[33]    A. Guerrero, G. Garcia-Belmonte, I. Mora-Sero, J. Bisquert, Y. S. Kang, T. J. Jacobsson, J. P. Correa-Baena, A. Hagfeldt, *J. Phys. Chem. C* **2016**, *120*, 8023.

[34]    D. Klotz, G. Tumen-Ulzii, C. Qin, T. Matsushima, C. Adachi, *RSC Adv.* **2019**, *9*, 33436.

[35]    S. Tsarev, I. K. Yakushchenko, S. Y. Luchkin, P. M. Kuznetsov, R. S. Timerbulatov, N. N. Dremova, L. A. Frolova, K. J. Stevenson, P. A. Troshin, *Sustain. Energy Fuels* **2019**, *3*, 2627.